A new halocarbon absorption model based on HITRAN cross-section data and new estimates of halocarbon instantaneous clear-sky radiative forcing

Stefan A. Buehler[1], Manfred Brath[1], Oliver Lemke[1], Øivind Hodnebrog[2], Robert Pincus[3], Patrick Eriksson[4], Iouli Gordon[5], and Richard Larsson[1]

[1]Meteorologisches Institut, Centrum für Erdsystem- und Nachhaltigkeitsforschung (CEN), Fachbereich Erdsystemwissenschaften, Fakultät für Mathematik, Informatik und Naturwissenschaften, Universität Hamburg, Bundesstrasse 55, 20146 Hamburg, Germany

[2]Center for International Climate Research (CICERO), Oslo, Norway

[3]Lamont-Doherty Earth Observatory, Columbia University, Palisades NY, USA

[4]Department of Space, Earth and Environment, Chalmers University of Technology, Gothenburg, Sweden

[5]Atomic and Molecular Physics Division, Center for Astrophysics, Harvard & Smithsonian

Key Points:

- A new polynomial model for laboratory absorption cross-section data was developed.
- The new model was used to compute instantaneous clear-sky halocarbon radiative efficiencies and present day radiative forcing.
- Halocarbons are found to contribute approximately 20% of the total anthropogenic instantaneous clear-sky forcing.

Corresponding author: Stefan A. Buehler, `stefan.buehler@uni-hamburg.de`

Abstract

The article describes a new practical model for the infrared absorption of chlorofluorocarbons and other gases with dense spectra, based on HITRAN absorption cross-sections. The model is very simple, consisting of frequency-dependent polynomial coefficients describing the pressure and temperature dependence of absorption. Currently it is implemented for the halocarbon species required by the Radiative Forcing Model Intercomparison Project (RFMIP). This approach offers practical advantages compared to previously available options, and is traceable, since the polynomial coefficients follow directly from the laboratory spectra.

The model is applied to the problem of computing instantaneous clear-sky halocarbon radiative efficiencies and present day radiative forcing. Results are in reasonable agreement with earlier assessments that were carried out with the less explicit Pinnock method, and thus broadly validate that method. Overall, halocarbons are responsible for a substantial share of the present-day forcing, $0.573\,\mathrm{Wm}^{-2}$ (instantaneous clear-sky at the TOA), corresponding to approximately 20% of the total anthropogenic forcing, or 44% compared to anthropogenic CO_2 forcing alone.

Plain Language Summary

Chlorofluorocarbons and other related gases have dense and complicated absorption spectra that can be measured in the laboratory. We bring such measurements to a form that can be used for simulations of the transfer of radiation through the atmosphere. Then we use the new model to calculate new estimates of the climate impact of these man-made gases. Neglecting complications by clouds and fast atmospheric adjustments, we find that they are responsible for 20% of the total man-made increase in greenhouse effect.

1 Introduction

In this work, we present a simple new model of halocarbon absorption, based on laboratory measurements collected by HITRAN (Gordon et al., 2017; Kochanov et al., 2019), and use it to estimate present-day instantaneous clear-sky halocarbon climate forcing and radiative efficiencies of the different compounds.

The need for the new model arises because spectroscopic data to date come in two different forms, depending on molecular species. The more physically sound form is as catalogues of spectral line parameters, from which the total absorption cross-section for arbitrary frequency, pressure and temperature can be calculated as the sum over all spectral lines. But such catalogues are not yet available for many molecular species with dense spectra.

The other form of data are as measured absorption cross-sections at a discrete set of pressures (p) and temperatures (T). This solves the problem of not being able to handle the complexity of the line spectrum, but instead raises the problem how to estimate absorption for p / T conditions that are different from those of the measurements. In the atmosphere, variations in p and T are large (five orders of magnitude for p and still 100 K or 50% for T), and in general one has to know the local absorption cross-sections in order to simulate the radiative transfer trough the atmosphere accurately. This requires the discrete absorption cross-section data to be cast into the form of a model that provides absorption as a continuous function of frequency, p and T, just like the calculation from spectral line parameters does for species for which it is available. Such a model has many applications, for example in remote sensing, in generating k-distributions for circulation model radiation schemes, and in estimating radiative forcing.

Some available RT models, such as LBLRTM (Clough et al., 2005) and SFIT (Hase et al., 2004) do already contain such functions internally for selected molecules, but the list has been incomplete and the implementation of these models has not been very transparent, so that we see the need for a new model. For this purpose, we transform the HITRAN laboratory cross-sections data (Gordon et al., 2017) into an absorption model by a simple second-order polynomial fit. This is done for all absorption species that are part of the RFMIP experiment (Pincus et al., 2016) in CMIP6 (Eyring et al., 2016). Almost all, that is, since we treat two species (CH_3Cl and CH_3Br) by explicit spectral line calculations, and one species (C_7F_{16}) not at all, because there is neither spectral line nor cross-section data available from HITRAN. The specification of gas concentrations in RFMIP follows the more general CMIP specification for concentrations (Meinshausen et al., 2017).

As a test and demonstration of the new model we consider the problem of estimating radiative forcing by halocarbons and related chemical compounds, which is an important part of the total anthropogenic climate forcing. Existing assessments (see review

in Hodnebrog, Aamaas, et al. (2020)) are based on the Pinnock method (Pinnock et al., 1995). In that method, forcing at some reference level (usually the tropopause) is pre-calculated for an artificial absorber that absorbs weakly with the same cross-section at all frequencies, and this is done for a dense frequency grid, obtaining what we call the Pinnock forcing curve. Forcing for an arbitrary molecular species can then be estimated by multiplying the Pinnock curve with the measured absorption cross-section of that species. The newest elaboration even takes into account stratospheric temperature adjustment in the Pinnock curve (Shine & Myhre, 2020), so that the method is one step closer to providing the effective radiative forcing (Hodnebrog, Myhre, et al., 2020).

While this method is very efficient, it has the disadvantage of using only the laboratory measurement at a single pressure and temperature. Often the measurement closest to surface pressure and room temperature is used, since the experimental uncertainties are typically smallest under those conditions. While it is easy to repeat the calculation with a different spectrum, the method in its present form can not account for the fact that the local absorption spectrum at different altitudes in reality depends on the local pressure and temperature. The method could probably be extended to take these variations into account, in analogy to the radiative kernel method that is used to diagnose radiative feedbacks and adjustments in climate models (Soden & Held, 2006), but that would significantly increase its computational cost and complexity.

Furthermore, radiative forcing has been shown to depend strongly on the atmospheric state at different locations on the globe (Huang et al., 2016) not just through the temperature dependence of the Planck function which governs emission, but also through the temperature dependence of absorption, and these dependencies are difficult to represent in the Pinnock method, which typically uses just a few atmospheres.

Here we apply the new halocarbon absorption model to a set of 100 reference atmospheres to compute new estimates of the global mean instantaneous clear-sky radiative forcing by halocarbons with the radiative transfer model ARTS (Buehler et al., 2018; Eriksson et al., 2011; Buehler et al., 2005). For simplicity, we refer to the new halocarbon model also with the name 'ARTS' below, where it is necessary to distinguish it from other models. But the halocarbon model itself is constructed such that it can be easily used in other radiative transfer models as well.

The paper is structured as follows: Section 2 describes the new absorption model and the philosophy behind it. Section 3 presents new estimates of instantaneous clear-sky radiative efficiency and present-day radiative forcing, based on our model and the RFMIP/CMIP gas concentrations. Section 4 contains the summary and conclusions.

2 Absorption Model

2.1 HITRAN Data

As outlined above, for many heavy polyatomic molecules, it is very difficult to provide accurate line-by-line lists due to the complexity of their spectra, and therefore an acceptable alternative practice is to publish absorption cross-sections at different pressures and temperatures, measured in the laboratory. Large sets of such data are described by Sharpe et al. (2004), Johnson et al. (2010) and Hodnebrog et al. (2013). HITRAN (the high-resolution transmission molecular absorption database) draws on such compilations, and complements them with numerous individual measurements from the literature, in order to provide measured absorption cross-sections for almost 300 different gas molecules. (Another database that systematically collects cross-sections in this way is GEISA (Jacquinet-Husson et al., 2016), but our study is based on the HITRAN data.)

These HITRAN cross-section data are described in detail in Gordon et al. (2017). We use the HITRAN2016 version. Note that a new version of HITRAN has become available since our model was implemented (HITRAN2020, released in October 2021, Gordon et al., 2022), featuring a few updates in cross-sections with respect to HITRAN2016. For instance, CFC-11 data were updated with recent measurements from Harrison (2018).

The structure of the data is such that for each absorption species there are data in one or more spectral bands, and for each spectral band there can be data at several pressure / temperature pairs. As an example, Figure 1 shows one such band for CFC11. This is one of the best-covered species, and the figure also shows the pressures and temperatures of the available CFC11 spectra for the band. Coverage can be much poorer for other species as shown in Figure 2. HALON1301, for example, is available at three different temperatures, but only ambient pressure, and HFC236fa has only a single measured spectrum at ambient pressure and temperature.

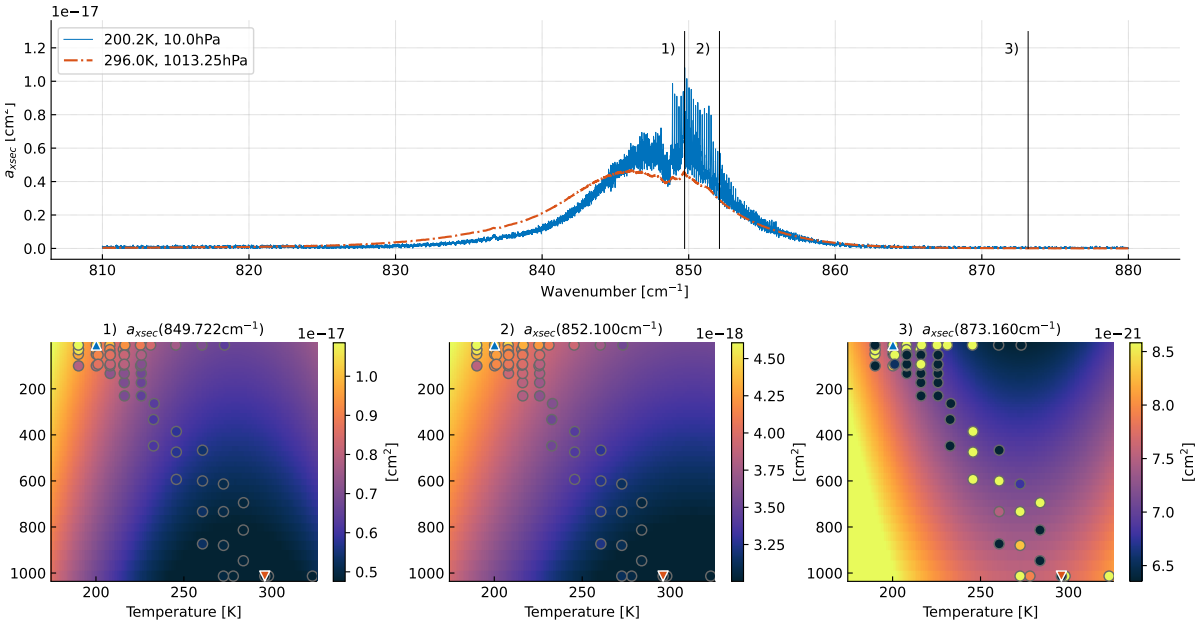

Figure 1. HITRAN laboratory absorption cross-section data of CFC11. The black vertical lines denote the wavenumbers of the three bottom plots. Bottom plots show fitted absorption cross-section as function of T and p. The circles denote the cross-sections from HITRAN laboratory data. The triangles show the position in pressure and temperature space of the spectra shown in the top plot. Note that the aparent discrepancies in the HITRAN data in the rightmost bottom plot represent noise, since the top plot shows that the absolute value there is very small.

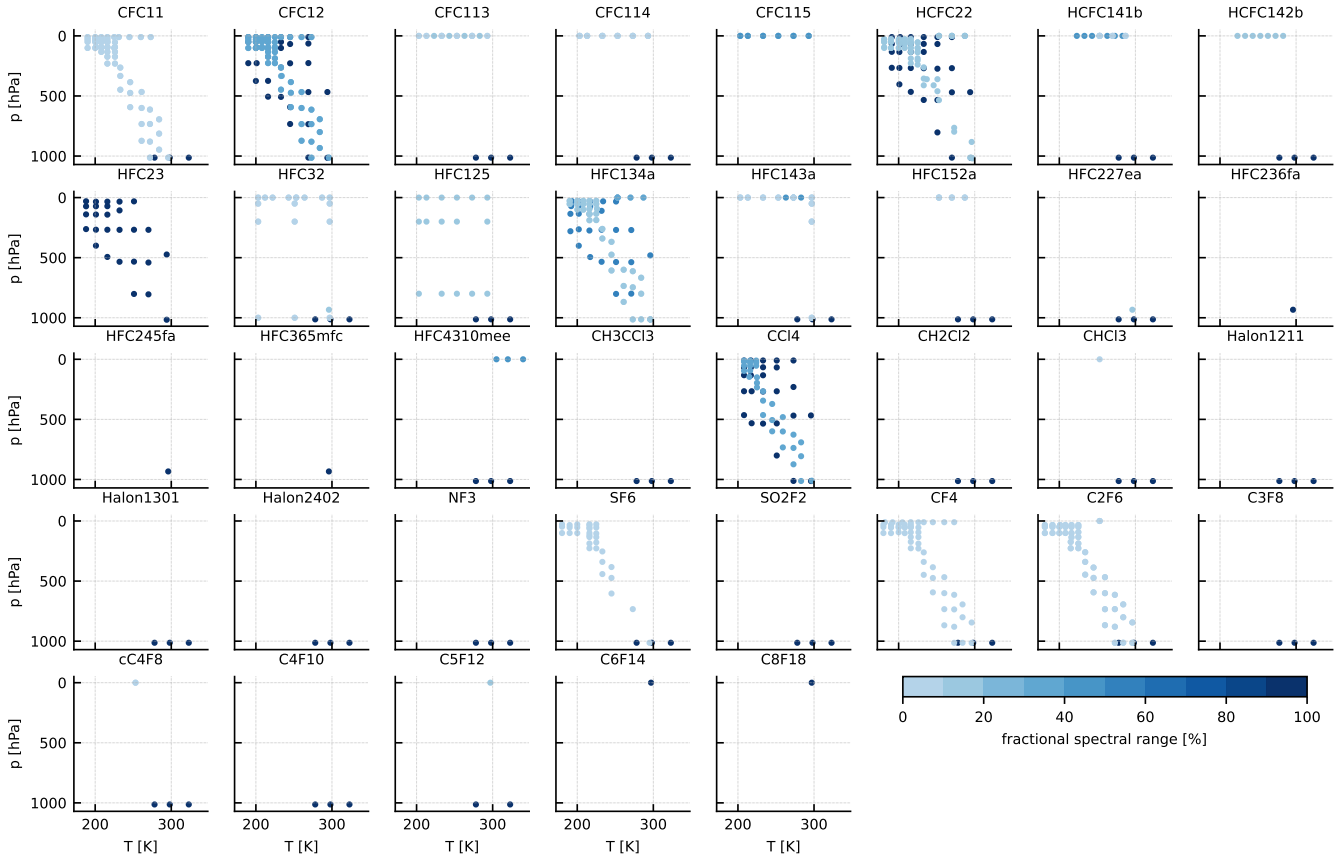

Figure 2. HITRAN absorption cross-section spectra for relevant molecules. Each dot represents an available spectrum. Spectra have varying frequency coverage. The color indicates the spectral range of each spectrum in relation to the spectral range of the fit.

2.2 Modeling Strategies

To use these data in an RT simulation, it is necessary to provide an estimate of the absorption at arbitrary frequency, temperature, and pressure, within reasonable limits, not just at the discrete points of the laboratory measurements. This is a practical challenge, since data often are rather sparsely sampled in pressure and temperature.

One approach to solve this is to start with a laboratory measurement at low pressure, and convolve it with a Lorentz function with a pressure dependent width to mimic the effect of pressure broadening. This approach, which we will refer to as the *convolution method*, is for example taken in LBLRTM (Clough et al., 2005).

We started out this project by systematically implementing the convolution method, i.e., we set up a simple model for the pressure dependence of the width (linear with a breakpoint) and determined suitable parameters for this model for those datasets with sufficient coverage of the laboratory data in pressure (p) / temperature (T) space. For other species we used a default pressure dependence.

This approach worked, but we were not fully satisfied with it. There are two main drawbacks: First, it is challenging to account for the temperature dependence, because the sampling of the available laboratory spectra in p / T space is so irregular that neither temperature interpolation before the convolution nor after the convolution gives reliable results in all cases. For example, it sometimes introduces artificial negative values. The second drawback of the convolution method is that it uses only a small part of the laboratory data for the actual model, since it relies heavily on the single low pressure reference spectrum.

We therefore also investigated the less physical and more pragmatic approach of fitting a suitable simple *polynomial model* to the entire set of measurements for a given species. This approach gives more accurate results, judged by how accurately the model reproduces the measurements and how well-behaved it is in those areas of p / T space that are not covered by any measurements. Based on these tests, the convolution method was given up and the polynomial model was selected as standard. It is described in more detail below. The approach of fitting a polynomial model is fairly common practice for ultraviolet absorption cross-sections (e.g. Eq. 1 in Bak et al., 2020), but as far as we know has not yet been used for the infrared spectral range. In the ultraviolet case it is only

the temperature dependence that is fitted, since pressure broadening is much less relevant than in the infrared, due to the dominant Doppler broadening.

An interesting alternative to our approach is the pseudo-line method (PL method from here on). In the PL method, the measured cross-sections are interpolated by a set of pseudo spectral lines, parameters of which are fitted so that they reproduce the measurements. This approach is quite wide-spread in remote sensing with Fourier transform instruments (e.g., Rinsland et al., 1985) and used in the popular SFIT retrieval software (Hase et al., 2004). However, PL parameters are not readily available for most of the halocarbon species investigated here.

Rather than attempting to derive new PL parameters for the HITRAN cross-section data, we chose the polynomial fit method for its greater simplicity, which makes the problem of deriving the parameterisation simultaneously for a long list of species tractable, whereas the PL method, at least in its present form, seems to need some expert judgment for each individual species. It would also need partition functions, which are not readily available for most of the species considered here.

2.3 The Polynomial Model

The basic idea is to set up a simple model for the pressure and temperature dependence of the absorption species, and then apply a global fit to all the available laboratory spectra for a given species. This is done separately for all frequencies where laboratory data are available. Explicitly, for a given species and at a given frequency ν, the observed cross-section $\sigma(T, p)$ is fitted in temperature T and pressure p by an up to 2nd order polynominal:

$$\sigma = c_{00} + c_{10}x + c_{01}y + c_{20}x^2 \tag{1}$$

with

$$x = \frac{T}{T_0}\,, \tag{2}$$

and

$$y = \frac{p}{p_0}\,, \tag{3}$$

using a least squares fit. The variables $T_0 = 1\,\mathrm{K}$ and $p_0 = 1\,\mathrm{Pa}$ are constant factors to remove the units of T and p. The coefficients c_{ij} and the cross-section σ are defined in units of [m^2]. The frequency dimension was omitted in the above equations for brevity,

Table 1. Fitting conditions for the cross-section fit. Variables x and y are defined according to Equations 2 and 3. Columns $N_{T,\min}$, $N_{p,\min}$ and $N_{\min}$ state the minimum required number of laboratory cross-section spectra in T, in p and in total. The last two columns state the required range in p and T, respectively.

fit model	$N_{T,\min}$ $N_{p,\min}$ $N_{\min}$ $\max(p) - \min(p) \geq$ $\max(T) - \min(T) \geq$				
$c_{00} + c_{10}x + c_{01}y + c_{20}x^2$	5	2	6	800 hPa	80 K
$c_{00} + c_{10}x + c_{01}y$	2	2	4	800 hPa	40 K
$c_{00} + c_{10}x + c_{20}x^2$	5	1	5	0 hPa	80 K
$c_{00} + c_{10}x$	3	1	3	0 hPa	40 K
$c_{00} + c_{01}y$	1	3	3	800 hPa	0 K
c_{00}	1	1	1	0 hPa	0 K

but note that the coefficients are given for a discreet set of frequencies. When the model is applied, absorption has to be interpolated in frequency between these discreet points.

The fitting process includes a simple outlier detection algorithm.

1. Fit the data using all given data at frequency ν.
2. Estimate the residuals between fit and data.
3. Fit the data excluding all data points with residuals $> 1.5\,\sigma_{data}$ in which σ_{data} is the standard deviation of the data at given frequency

The HITRAN cross-section data are very diverse in their spectral resolution, and in p / T coverage, as discussed in detail in Kochanov et al. (2019). For example, there are species that have high p / T resolution data in a specific spectral range and only coarse p / T resolution data outside that range. Frequency resolution also varies considerably in different parts of the spectrum. Spectra cover different frequency ranges, sometimes overlapping. Since the number of observations at different temperatures and pressures varies over the spectral range, the fitting model is selected for each frequency individually, as summarised in Table 1.

One advantage of this method is that the use of the absorption model in an RT code is extremely simple, basically just using Equation 1 with our tabulated fit coefficient data, where missing coefficients are set to zero. The evaluation of the model is computationally cheap, since no expensive operations, such as convolutions, are needed. In a final step, absorption cross-sections are linearly interpolated in frequency between the discrete model points.

Extrapolation is always more dangerous than interpolation, but we selected the interpolation order such that it is safe to use the new polynomial model also outside the p / T range of the laboratory measurements. This simplifies the implementation of the model, for example in a radiative transfer code.

One caveat is that negative absorption cross-sections can occur, both inside and outside the laboratory temperature and pressure range. Inside, the negative values occur only at the noise level of the absorption spectra. Outside, more negative values are possible due to the extrapolation. To account for both issues, negative absorption cross-sections are simply set to zero when the model is applied. To avoid a positive bias due to the removal of negative values, the spectrum is scaled afterwards so that the integral over the spectrum of the specific band does not change.

To fit the polynomial model, input data have to be harmonised with respect to their frequency grids. The basic idea is to use the highest spectral resolution of the set of observations of a species and use this resolution as the reference resolution. The observations with coarser frequency resolution are linearly interpolated onto this resolution.

Some molecular species have a very high resolution for a small spectral range, and coarse resolution or no data elsewhere. An interpolation to a uniform high-resolution grid therefore would be wasteful, and instead the data are split into bands of different spectral resolution. Table 2 and 3 list the implemented species, their bands, and for each band the p / T limits of the laboratory data and the polynomial orders in p and T that were adopted.

A good measure for the overall absorption strength of a molecule is the frequency-integrated absorption cross-section S. Table 4 lists this for our new polynomial model ('ARTS') and the raw HITRAN laboratory spectra. For ARTS we use 293 K and 1013.25 hPa, for HITRAN the spectra closest to these conditions. The new model does not agree exactly with the individual raw spectra, since spectra at other pressures and temperatures also influence the polynomial coefficients. Discrepancies are mostly below 1%, but in a few cases around 3% to 5% and in one case (HFC32) as large as approximately 7%.

These larger discrepancies in S for some models indicate that the fit quality is poorer for these species, which could be either due to inadequateness of the second order polynomial model, or due to inconsistencies / inhomogeneities of the HITRAN spectra at dif-

Table 2. Considered cross-section species together with spectral, pressure and temperature limits and with $O_{p,T}$ the maximum polynominal order of the pressure/temperature dependency of the band. (Continued in next table.)

species	band	$\widetilde{\nu}_{\min}$ [cm^{-1}]	$\widetilde{\nu}_{\max}$ [cm^{-1}]	$\delta\widetilde{\nu}$ [cm^{-1}]	$p_{\min}$ [hPa]	$p_{\max}$ [hPa]	$T_{\min}$ [K]	$T_{\max}$ [K]	O_p	O_T
CFC11	0	570	810	0.060	1013.25	1013.25	278.10	323.10	0	1
	1	810	880	0.003	10.00	1013.25	190.00	323.10	1	2
	2	880	1050	0.060	1013.25	1013.25	278.10	323.10	0	1
	3	1050	1120	0.003	10.00	1013.25	190.00	323.10	1	2
	4	1120	6500	0.060	1013.25	1013.25	278.10	323.10	0	1
CFC12	0	800	1270	0.001	10.00	1014.58	189.50	296.30	1	2
CFC113	0	600	1250	0.015	0.00	1013.25	203.00	323.10	1	2
	1	1250	5000	0.060	1013.25	1013.25	278.10	323.10	0	1
CFC114	0	600	815	0.060	1013.25	1013.25	278.10	323.10	0	1
	1	815	860	0.015	0.00	1013.25	203.00	323.10	1	2
	2	860	870	0.060	1013.25	1013.25	278.10	323.10	0	1
	3	870	960	0.015	0.00	1013.25	203.00	323.10	1	2
	4	960	1030	0.060	1013.25	1013.25	278.10	323.10	0	1
	5	1030	1067	0.015	0.00	1013.25	203.00	323.10	1	2
	6	1067	1095	0.060	1013.25	1013.25	278.10	323.10	0	1
	7	1095	1285	0.015	0.00	1013.25	203.00	323.10	1	2
	8	1285	5000	0.060	1013.25	1013.25	278.10	323.10	0	1
CFC115	0	955	1015	0.015	0.00	0.00	203.00	293.00	0	2
	1	1110	1145	0.015	0.00	0.00	203.00	293.00	0	2
	2	1167	1260	0.015	0.00	0.00	203.00	293.00	0	2
HCFC22	0	730	1380	0.001	0.00	1019.38	181.00	297.00	1	2
HCFC141b	0	550	560	0.060	1013.25	1013.25	278.10	323.10	0	1
	1	560	3100	0.008	0.00	1013.25	223.00	323.10	1	2
	2	3100	6500	0.060	1013.25	1013.25	278.10	323.10	0	1
HCFC142b	0	600	650	0.060	1013.25	1013.25	278.10	323.10	0	1
	1	650	1500	0.008	0.00	1013.25	223.00	323.10	1	2
	2	1500	6500	0.060	1013.25	1013.25	278.10	323.10	0	1
HFC23	0	950	1500	0.001	30.66	1016.45	187.60	294.40	1	2
HFC32	0	400	450	0.120	933.26	933.26	296.00	296.00	0	0
	1	450	630	0.017	0.00	1013.25	253.00	323.10	1	1
	2	630	995	0.060	933.26	1013.25	278.10	323.10	0	1
	3	995	1236	0.015	0.00	1013.25	203.00	323.10	1	2
	4	1236	1385	0.060	933.26	1013.25	278.10	323.10	0	1
	5	1385	1475	0.015	0.00	1013.25	203.00	323.10	1	2
	6	1475	6500	0.060	1013.25	1013.25	278.10	323.10	0	1
HFC125	0	495	495	0.048	0.00	0.00	253.00	253.00	0	0
	1	495	499	0.048	0.00	799.93	203.00	273.00	0	1
	2	499	1504	0.048	0.00	1013.25	203.00	323.10	1	2
	3	1504	6500	0.060	1013.25	1013.25	278.10	323.10	0	1
HFC134a	0	75	590	0.017	0.00	0.00	253.00	253.00	0	0
	1	600	750	0.015	0.00	0.00	253.00	253.00	0	0
	2	750	1600	0.001	0.00	1014.32	190.00	296.00	1	2
HFC143a	0	500	550	0.060	1013.25	1013.25	278.10	323.10	0	1
	1	550	3500	0.008	0.00	1013.25	203.00	323.10	1	2
	2	3500	6500	0.060	1013.25	1013.25	278.10	323.10	0	1
HFC152a	0	525	830	0.060	1013.25	1013.25	278.10	323.10	0	1
	1	830	840	0.010	0.00	1013.25	253.00	323.10	1	1
	2	840	995	0.009	0.00	1013.25	253.00	323.10	1	1
	3	995	1050	0.010	0.00	1013.25	253.00	323.10	1	1
	4	1050	1205	0.009	0.00	1013.25	253.00	323.10	1	1
	5	1205	1320	0.010	0.00	1013.25	253.00	323.10	1	1
	6	1320	1490	0.009	0.00	1013.25	253.00	323.10	1	1
	7	1490	1500	0.010	0.00	1013.25	253.00	323.10	1	1
	8	1500	6500	0.060	1013.25	1013.25	278.10	323.10	0	1
HFC227ea	0	400	500	0.121	933.26	933.26	296.00	296.00	0	0
	1	500	6500	0.060	933.26	1013.25	278.10	323.10	0	1
HFC236fa	0	350	1500	0.120	933.26	933.26	296.00	296.00	0	0
HFC245fa	0	640	1500	0.241	933.26	933.26	296.00	296.00	0	0
HFC365mfc	0	600	2000	0.060	933.26	933.26	296.00	296.00	0	0

Table 3. Considered cross-section species together with spectral, pressure and temperature limits and with $O_{p,T}$ the maximum polynominal order of the pressure/temperature dependency of the band. (Continuation of previous table.)

species	band	$\widetilde{\nu}_{\min}$ [cm^{-1}]	$\widetilde{\nu}_{\max}$ [cm^{-1}]	$\delta\widetilde{\nu}$ [cm^{-1}]	$p_{\min}$ [hPa]	$p_{\max}$ [hPa]	$T_{\min}$ [K]	$T_{\max}$ [K]	O_p	O_T
HFC4310mee	0	500	550	0.060	1013.25	1013.25	278.10	323.10	0	1
	1	550	3500	0.030	0.00	1013.25	278.10	340.00	1	1
	2	3500	6500	0.060	1013.25	1013.25	278.10	323.10	0	1
CH3CCl3	0	500	6500	0.060	1013.25	1013.25	278.10	323.10	0	1
CCl4	0	700	860	0.001	10.00	1013.25	207.90	296.70	1	2
CH2Cl2	0	600	6500	0.060	1013.25	1013.25	278.10	323.10	0	1
CHCl3	0	580	725	0.060	1013.25	1013.25	278.10	323.10	0	1
	1	725	805	0.048	0.00	1013.25	253.00	323.10	1	1
	2	805	7200	0.060	1013.25	1013.25	278.10	323.10	0	1
Halon1211	0	600	6500	0.060	1013.25	1013.25	278.10	323.10	0	1
Halon1301	0	510	6500	0.060	1013.25	1013.25	278.10	323.10	0	1
Halon2402	0	550	6500	0.060	1013.25	1013.25	278.10	323.10	0	1
NF3	0	600	6500	0.060	1013.25	1013.25	278.10	323.10	0	1
SF6	0	560	925	0.060	1013.25	1013.25	278.10	323.10	0	1
	1	925	955	0.005	26.93	1013.52	180.00	323.10	1	2
	2	955	6500	0.060	1013.25	1013.25	278.10	323.10	0	1
SO2F2	0	500	6500	0.060	1013.25	1013.25	278.10	323.10	0	1
CF4	0	570	1250	0.060	1013.25	1013.25	278.10	323.10	0	1
	1	1250	1290	0.003	10.05	1014.58	180.40	323.10	1	2
	2	1290	6500	0.060	1013.25	1013.25	278.10	323.10	0	1
C2F6	0	500	680	0.060	1013.25	1013.25	278.10	323.10	0	1
	1	680	750	0.015	0.00	1013.25	253.00	323.10	1	1
	2	750	1061	0.060	1013.25	1013.25	278.10	323.10	0	1
	3	1061	1165	0.003	0.00	1013.65	180.60	323.10	1	2
	4	1165	1170	0.060	1013.25	1013.25	278.10	323.10	0	1
	5	1170	1220	0.030	0.00	1013.25	253.00	323.10	1	1
	6	1220	1285	0.003	0.00	1013.65	180.60	323.10	1	2
	7	1285	1380	0.030	0.00	1013.25	253.00	323.10	1	1
	8	1380	6500	0.060	1013.25	1013.25	278.10	323.10	0	1
C3F8	0	600	6500	0.060	1013.25	1013.25	278.10	323.10	0	1
cC4F8	0	550	555	0.061	1013.25	1013.25	278.10	323.10	0	1
	1	555	590	0.015	0.00	1013.25	253.00	323.10	1	1
	2	590	900	0.060	1013.25	1013.25	278.10	323.10	0	1
	3	900	1460	0.015	0.00	1013.25	253.00	323.10	1	1
	4	1460	6500	0.060	1013.25	1013.25	278.10	323.10	0	1
C4F10	0	500	6500	0.060	1013.25	1013.25	278.10	323.10	0	1
C5F12	0	500	700	0.060	1013.25	1013.25	278.10	323.10	0	0
	1	700	1400	0.012	0.00	1013.25	278.10	323.10	0	1
	2	1400	6500	0.060	1013.25	1013.25	278.10	323.10	0	0
C6F14	0	700	1400	0.012	0.00	0.00	297.00	297.00	0	0
C8F18	0	700	1400	0.012	0.00	0.00	297.00	297.00	0	0

Table 4. Integrated absorption cross-sections. The S columns are integrated absorption cross-sections for HITRAN, the new ARTS model, and Hod20. The latter are the values given in the appendix for the database 'H16' (HITRAN 2016) so they should be based on exactly the same data as ours. For a few species, where there is no 'H16' value in Hod20, another suitable entry is used. These are documented in the footnotes of Table 5. The last two columns show percentage differences relative to HITRAN and Hod20.

Species	S_{HITRAN} $[10^{-17}\mathrm{cm}^2\mathrm{cm}^{-1}]$	S_{ARTS} $[10^{-17}\mathrm{cm}^2\mathrm{cm}^{-1}]$	S_{Hod} $[10^{-17}\mathrm{cm}^2\mathrm{cm}^{-1}]$	$\Delta_{\mathrm{ARTS-HITRAN}}$ [%]	$\Delta_{\mathrm{ARTS-Hod}}$ [%]
CFC11	10.06	10.04	10.10	-0.22	-0.62
CFC12	13.51	13.59	13.50	0.57	0.64
CFC113	14.59	14.41	14.60	-1.20	-1.28
CFC114	17.39	17.40	17.40	0.07	-0.01
CFC115	12.10	12.09	12.10	-0.08	-0.09
HCFC22	10.48	10.52	10.50	0.35	0.15
HCFC141b	8.56	8.50	8.40	-0.69	1.24
HCFC142b	11.40	11.40	11.20	0.01	1.79
HFC23	12.28	12.28	12.30	-0.00	-0.14
HFC32	6.65	7.13	7.00	7.14	1.85
HFC125	17.53	17.69	17.40	0.94	1.68
HFC134a	14.11	14.02	13.20	-0.64	6.24
HFC143a	14.14	14.21	13.80	0.46	2.97
HFC152a	8.45	8.46	8.00	0.21	5.81
HFC227ea	25.40	25.16	25.30	-0.95	-0.54
HFC236fa	22.81	22.81	22.80	0.00	0.05
HFC245fa	19.57	19.57	19.60	0.00	-0.17
HFC365mfc	18.75	18.75	18.80	0.00	-0.29
HFC4310mee	30.51	30.81	30.40	1.00	1.36
CH3CCl3	5.53	5.52	5.30	-0.23	4.06
CCl4	6.73	6.54	6.70	-2.74	-2.33
CH2Cl2	2.95	2.95	2.80	0.02	5.43
CHCl3	5.02	5.06	5.00	0.70	1.19
Halon1211	13.24	13.30	13.20	0.50	0.79
Halon1301	16.09	16.90	16.10	4.99	4.94
Halon2402	16.14	16.20	16.10	0.38	0.63
NF3	7.23	7.26	7.20	0.43	0.86
SF6	20.93	21.18	21.20	1.23	-0.08
SO2F2	14.04	13.91	14.00	-0.93	-0.66
CF4	20.14	20.09	19.80	-0.27	1.46
C2F6	22.76	22.90	23.10	0.61	-0.87
C3F8	27.51	27.00	27.50	-1.83	-1.80
cC4F8	21.73	21.74	21.70	0.04	0.19
C4F10	32.45	32.43	32.40	-0.08	0.09
C5F12	37.34	37.61	37.30	0.72	0.83
C6F14	38.54	38.54	38.50	0.00	0.11
C8F18	45.55	45.55	45.60	0.00	-0.10

ferent p / T conditions. Our educated guess is that the latter is more likely, so it would be worthwhile (but beyond the scope of this article) to examine these species more closely from a spectroscopic consistency point of view.

The problem of fit consistency and data homogeneity is illustrated by Figure 3, showing S as a function of T for two different species. For CFC11 there is a wealth of data, lending confidence to the quadratic fit. In contrast, for Halon1301 there are only three measurements, near 280 K, 300 K and 320 K. The middle one is significantly lower. Taking this at face value leads to a strong T dependence, so strong that it would impact forcing estimates significantly, even if one were to extrapolate linearly outside the T range of the data. We judge a single measurement as insufficient to support such a drastic model, so we instead select the linear fit for this species, leading to a higher fit residual, and a model with hardly any T dependence.

Another reason for larger discrepancies in some cases are ambiguities in which of the laboratory spectra to use for the S_{HITRAN} calculation, since different spectral datasets have different p / T ranges, as shown in Table 2. The spectrum closest to ambient conditions may not cover the full spectral range. The algorithm that we use is that we split the HITRAN spectra according to our defined frequency bands. For each band we take the HITRAN dataset that is closest to ambient conditions and covers at least 90% of the band. Note that the S_{ARTS} calculations do not suffer from this ambiguity, since one can simply use the model at the prescribed p / T.

Table 4 also lists S values quoted for HITRAN 2016 in the supplement of Hodnebrog, Aamaas, et al. (2020), which we will refer to as Hod20 from now on. These are based on the same dataset that we use so the numbers should be comparable. Indeed, discrepancies between S_{ARTS} and S_{Hod} are mostly below 1%. In a few cases they are around 2–6%.

A possible issue affecting the S value is zeroing of negative laboratory absorption data, which is done in the default HITRAN data, but not in an alternative data version, also available from HITRAN. However, both this work and Hod20 use the default version (without negative values), ruling out that source of discrepancy.

In the case of the bigger discrepancies, the S_{Hod} value is lower (HFC134a, HFC152a, CH_3CCl_3, CH_2Cl_2, Halon1301). For Halon1301, the reason is the inconsistency of the

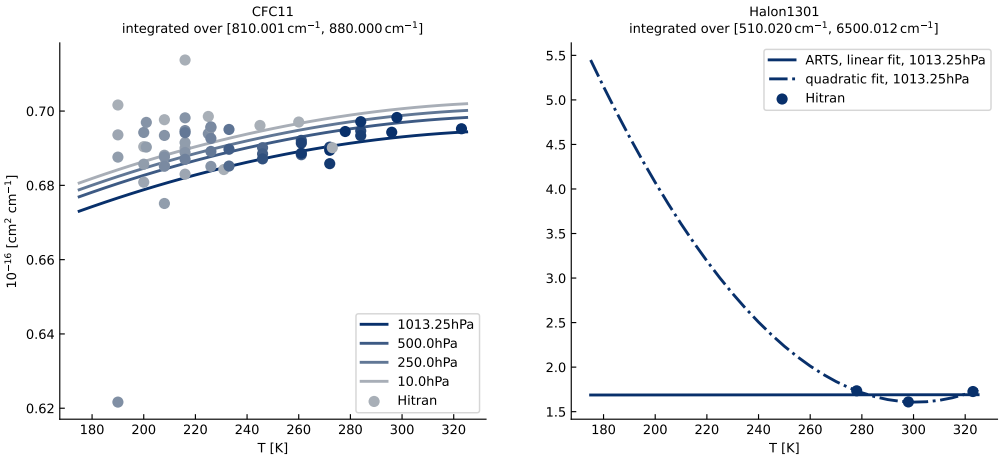

Figure 3. Integrated absorption cross-sections as a function of temperature for CFC11 and Halon1301. Lines denote fitted absorption cross-sections, circles denote HITRAN observations, color shading indicates pressure. For Halon1301 the integrated absorption cross-section when using a quadratic fit instead of a linear fit is also shown.

HITRAN cross-section data at different temperatures, discussed above. For the rest of these species, the reason is the smaller frequency range used in Hod20 for the S calculation (compare ranges given in Tables 2–3 to those given in the Hod20 supplement). Limiting the S_{ARTS} calculation to the Hod20 frequency range for these species results in differences below 1%. It should be noted that these S differences due to integration frequency range do not directly affect radiative forcing, since the frequency ranges omitted in Hod20 are either so high that they contribute little to the forcing (far away from the peak of the Planck function), or, in the case of HFC134a, masked by the CO_2 band.

3 Forcing Estimates

The new absorption model was used to estimate instantaneous clear-sky radiative efficiencies and present day radiative forcing of the different trace gases considered. Radiative forcing is defined here as the reduction in outgoing broadband (spectrally-integrated) longwave radiation when the concentration of the species is increased by some amount from a reference value, and is given in units of W m^{-2}. Radiative efficiency is the forcing divided by the concentration of the gas species, given in units of W m^{-2} ppb^{-1}. For gases with very small concentrations and thus small optical depths, as the ones considered here, the efficiency is a good measure of the strength of their radiative effect, since

the impact on radiation is linear in concentration. (For more abundant gases the radiative effect behaves non-linearly, so this concept is not applicable.)

In the spirit of RFMIP (Pincus et al., 2016), we concentrate on the simple instantaneous clear-sky case. Instantaneous meaning that we do not apply a stratospheric adjustment, clear-sky meaning that we do not include clouds in the calculation. We also do not apply any corrections for the lifetime of the gas species. These corrections are discussed briefly in Hod20, and in more detail in (Hodnebrog et al., 2013).

3.1 Atmospheric Scenarios and RT Model Setup

For RFMIP, a set of 100 atmospheres and corresponding averaging weights was developed in order to minimize sampling error in estimates of present-day to pre-industrial forcing by all greenhouse gases, not only in the global mean at the top of the atmosphere but regionally and at various levels in the atmosphere (Pincus et al., 2020). The same set of atmospheres and weights was used here. The standard error from the averaging can be used as a conservative estimate of the deviation of this mean value from the true global mean, which is found to be always below approximately 5%. Simulations were done for the scenarios 'present day' and 'preindustrial' of RFMIP/CMIP (Pincus et al., 2016; Meinshausen et al., 2017). Atmospheric conditions are given at 61 pressure levels from the surface to 0.01 Pa. With a few exceptions (CCl_4, CH_3Cl, CH_2Cl_2, $CHCl_3$, CH_3Br, CF_4), halocarbon concentrations are zero in the preindustrial scenario.

The Atmospheric Radiative Transfer Simulator (ARTS, version 2.5, (Buehler et al., 2018; Eriksson et al., 2011; Buehler et al., 2005)) was used for the forcing and radiative efficiency estimates. As outlined in Section 1, we calculate the forcing by doing one reference simulation of radiation fluxes and then, for each gas, one simulation where that gas is removed. This was done for all 100 atmospheres, then averaged with the correct RFMIP weights.

Fluxes were calculated using Gauss–Legendre quadrature with 3 radiation streams per hemisphere and with a frequency resolution of $0.05\,\mathrm{cm}^{-1}$ (64801 individual frequencies in the interval 10–3250 cm^{-1}). We evaluate them at the surface (SFC), at the top of the atmosphere (TOA), and at the tropopause (TRP), using the WMO definition for the latter.

Absorbing species were modeled either from spectral line data or with the new polynomial model based on the HITRAN laboratory cross-section. Spectral line species were H_2O, O_2, O_3, N_2, CO, CO_2, CH_4, N_2O, CH_3Br, and CH_3Cl. Additionally, CKD_MT version 2.5.2 absorption continua (Mlawer et al., 2012) were included for H_2O, N_2 and CO_2 (but no CO_2 line mixing), and the CKD_MT version 1.0 continuum was included for O_2.

3.2 Radiative Efficiencies

Figure 4a shows instantaneous clear-sky radiative efficiencies (REs) at the TOA. The blue bars mark a calculation where the spectrum at the fixed surface temperature and surface pressure is used throughout the atmosphere, as in earlier assessments (Hodnebrog, Aamaas, et al., 2020, and references therein). Where the available data allow it, we have parameterised the T dependence (red bars) or the T and p dependence (orange bars), as described above. Figure 4b shows the relative difference of the other bars from the blue bars.

As the figure shows, the p / T dependence leads to differences of up to approximately 8% in some cases. Unfortunately, laboratory data are not extensive enough for the p / T fit for many species, so it is likely that more species are affected by this than shown by the figure. For example, as discussed above, Halon1301 would have a very strong T dependence if we were to take the sparse laboratory data at face value. (We did the calculation also with the quadratic fit and linear extrapolation, and it leads to a 40% higher radiative efficiency.)

Table 5 summarises all radiative efficiencies (REs) calculated with our model. Compared to Figure 4, it includes two additional molecular species for completeness, CH_3Br and CH_3Cl, which we have calculated from spectral line data, not with the cross-section model.

Our focus is on the new halocarbon absorption model, not on providing the most realistic estimate of the most climatically-relevant radiative efficiency. We therefore focus on the instantaneous clear-sky forcing, ignoring stratospheric adjustment and clouds. The table gives this in the first two columns, at the top of the atmosphere and at the TRP. For the sake of comparison with Hod20 we also make a very rough estimate of the all-sky value at the tropopause by simply multiplying the clear-sky value with 0.75, the ratio between instantaneous values at the tropopause with and without clouds that Myhre

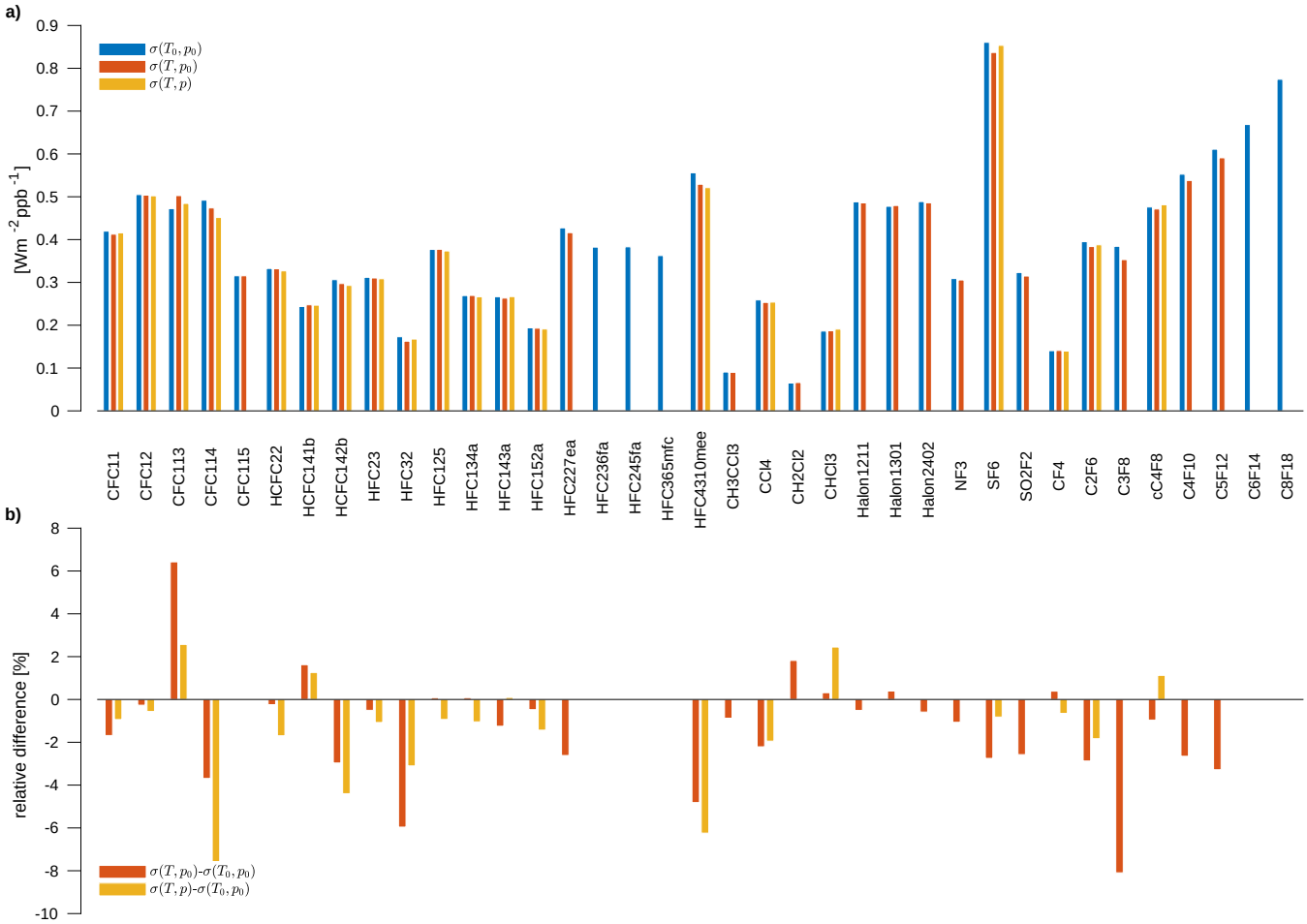

Figure 4. Radiative efficiency at the TOA, comparing our default model with temperature and pressure dependence $\sigma(T, p)$ to simplified models with only temperature dependence $\sigma(T, p_0)$ or no dependence at all $\sigma(T_0, p_0)$. The values of the default parameters are $T_0 = 293\,\mathrm{K}$ and $p_0 = 1013\,\mathrm{hPa}$, so the last case corresponds to other studies such as Hod20 that just use the laboratory spectra at ambient temperature and surface pressure. The available laboratory data do not always allow the temperature fit, and even more rarely the pressure fit. This can be seen from the available bar colors in the top figure (and also from Table 2). In those cases our model does not include those dependencies.

Table 5. Instantaneous radiative efficiencies in units of $Wm^{-2}ppb^{-2}$. The first four numerical columns contain the clear-sky value at the top of the atmosphere ('clear TOA'), the clear-sky value at the tropopause ('clear TRP'), the all sky value at the tropopause ('all-sky TRP', simply estimated as 0.75 times the clear TRP value), and the corresponding value given in the Appendix of Hod20 as 'New inst. RE' for the H16 (HITRAN 2016) database ('Hod.'). The last column contains the relative difference of the Hod20 value to our 'all-sky TRP' value.

Species	Clear TOA	Clear TRP	all-sky TRP	Hod.	Diff. Hod.
Chlorofluorocarbons					
CFC11	0.408	0.354	0.265	0.263	-1%
CFC12	0.493	0.423	0.317	0.299	-6%
CFC113	0.475	0.422	0.316	0.301	-5%
CFC114	0.443	0.399	0.299	0.310	4%
CFC115[a]	0.310	0.267	0.200	0.186	-7%
Hydrochlorofluorocarbons					
HCFC22	0.321	0.280	0.210	0.201	-4%
HCFC141b	0.242	0.217	0.162	0.158	-3%
HCFC142b	0.287	0.246	0.184	0.179	-3%
Hydrofluorocarbons					
HFC23	0.303	0.259	0.194	0.180	-7%
HFC32	0.165	0.147	0.110	0.115	4%
HFC125	0.367	0.313	0.234	0.220	-6%
HFC134a	0.262	0.226	0.169	0.157	-7%
HFC143a	0.262	0.222	0.167	0.157	-6%
HFC152a	0.188	0.162	0.122	0.115	-6%
HFC227ea	0.409	0.352	0.264	0.256	-3%
HFC236fa[b]	0.375	0.319	0.240	0.223	-7%
HFC245fa[c]	0.376	0.328	0.246	0.228	-7%
HFC365mfc[d]	0.356	0.304	0.228	0.213	-7%
HFC4310mee	0.512	0.446	0.335	0.330	-1%
Chlorocarbons and hydrochlorocarbons					
CH3CCl3	0.088	0.088	0.066	0.069	5%
CCl4	0.249	0.222	0.167	0.174	4%
CH3Cl[e]	0.008	0.008	0.006	0.006	-1%
CH2Cl2	0.065	0.061	0.046	0.047	2%
CHCl3	0.187	0.167	0.126	0.121	-4%
Bromocarbons, hydrobromocarbons and halons					
CH3Br[f]	0.006	0.005	0.004	0.006	57%
Halon1211	0.477	0.410	0.308	0.293	-5%
Halon1301	0.471	0.405	0.303	0.269	-11%
Halon2402	0.477	0.426	0.320	0.305	-5%
Fully fluorinated species					
NF3	0.300	0.260	0.195	0.189	-3%
SF6	0.838	0.715	0.536	0.518	-3%
SO2F2	0.309	0.272	0.204	0.207	2%
CF4	0.137	0.122	0.092	0.092	0%
C2F6	0.381	0.328	0.246	0.240	-3%
C3F8	0.347	0.326	0.245	0.253	3%
cC4F8	0.472	0.403	0.303	0.279	-8%
C4F10	0.528	0.458	0.344	0.337	-2%
C5F12	0.580	0.509	0.381	0.370	-3%
C6F14[g]	0.656	0.568	0.426	0.407	-5%
C8F18[h]	0.760	0.660	0.495	0.471	-5%
Mean difference					-1.6%

[a] Hod20 value is from row labeled 'H08', based on same laboratory data.

[b] Hod20 value is from row labeled 'Sihra et al. (2001)', based on same laboratory data.

[c] Hod20 value is from row labeled 'Sihra et al. (2001)', based on same laboratory data.

[d] Hod20 value is from row labeled 'Inoue et al. (2008)', based on same laboratory data.

[e] Our value is based on explicit spectral line calculations, Hod20 value is from row labeled 'Wallington et al. (2016)'.

[f] Our value is based on explicit spectral line calculations, Hod20 value is from row labeled 'PNNL'.

[g] Hod20 value is from row labeled 'Bravo et al. (2010)', based on same laboratory data.

[h] Hod20 value is from row labeled 'Bravo et al. (2010)', based on same laboratory data.

et al. (2006) find for CFC12. This value is also consistent with the range of clear-sky to all-sky conversion factors in Table 3 of (Pincus et al., 2020).

We can compare the new RE values with those given in the electronic supplement of Hod20, focusing on the values for HITRAN 2016, the database we use. Of the given forcing quantities, the Hod20 value for the new instantaneous RE is most comparable to our all-sky TRP value. Table 5 therefore lists these values for comparison, as well as their relative difference to ours.

It is important to note that Hodnebrog et al. use the Pinnock method, using only halocarbon spectra at surface pressure and ambient temperature, whereas we parameterise the absorption dependence in p / T space where possible, as discussed above.

On average, our values are 1.6% higher than those of Hod20, but there is one species, CH_3Br, for which our value is 57% lower. This is one of the two species for which HITRAN absorption cross-sections are not available and that we have therefore calculated from spectral line data. Normally one would trust the explicit spectral line calculation more than the cross-sections, but in this case examination of the catalog reveals that the HITRAN line parameter list for CH_3Br is incomplete. The relevant band at $600\,\mathrm{cm}^{-1}$ is missing completely, as can also be seen in Figure 2 of Kochanov et al. (2015). HITRAN plans to complete these data in the near future.

This problem only affects CH_3Br, and agreement is much better, 1%, for CH_3Cl, the other species that we have computed from spectral line data. Ignoring the outlier CH_3Br, our values are on average approximately 3% higher than those of Hod20. Again with the exception of CH_3Br, all differences are below approximately 10%. We consider this level of agreement as very good given the differences in methodology.

The most obvious factors contributing to the differences for individual species are (a) different integrated halocarbon absorption coefficient S, (b) the missing temperature dependence in the Hod20 calculations, (c) the atmospheric states (100 RFMIP profiles versus 2 profiles), (d) our crude clear-sky to all sky correction and (e) the tropopause definition used.

From Table 4 and the accompanying discussion, we conclude that factor a should not play a significant role except for the few cases where HITRAN data at different temperatures are most inconsistent (HFC32, CCl_4, Halon1301), where it could contribute

a few percent. From Figure 4 and the accompanying discussion we conclude that factor b can also contribute a few percent to the difference, in particular for CFC114 and HFC4310mee. A similar contribution from the remaining factors c–e is plausible. There also likely is significant cancellation of errors, as the factors are uncorrelated.

3.3 Present Day Forcing

Table 6 shows the present-day instantaneous clear-sky radiative forcings of the different species investigated. As Table 5, it includes CH_3Br and CH_3Cl for completeness, calculated from spectral line data, not with the cross-section model.

Our present-day forcing values are higher than those given in Table 4 of Hod20 but the numbers cannot be compared directly, since theirs are all-sky, include stratospheric adjustment, and include a lifetime correction. Of these three factors the first and third act to reduce their value, whereas the second acts to increase it.

Despite these differences, the ranking of forcing strength of the different species is remarkably consistent. The most significant difference in ranking is that in our calculation HFC125 has a weaker forcing than HFC23, whereas in theirs it is stronger. The reason for this difference is the assumed concentration of HFC125, which in the RFMIP/CMIP atmospheres that we used is only half of what is assumed in Hod20.

To put these results in perspective, Table 7 shows the corresponding forcings of the major greenhouse components, calculated by our model, using the same 100 RFMIP atmospheres and weights. Methodology is different here: Instead of leave-one-out calculations, the concentration profile of the component in question is replaced by its pre-industrial values. This is necessary because the optical depth of theses components is substantial, making forcing a non-linear function of concentration.

The last entry in Table 7 gives the forcing from a simulation where all halocarbons are replaced by their pre-industrial concentrations. The close agreement of this number with the sum-total of the leave-one-out halocarbon simulations (last entry in Table 6) confirms that nonlinearities are not an issue for the halocarbons.

For the major atmospheric absorbers, results in Table 7 are in excellent agreement with the results presented in Pincus et al. (2020), Table 2. Those are average numbers across the participating benchmark models, where our model ARTS was one of six, but

Table 6. Present-day radiative forcing by halocarbons. Columns 2 and 3 give the pre-industrial (PI) and present-day (PD) concentration, respectively. Remaining columns give the instantaneous clear-sky forcing (difference between PD and PI net fluxes) at the top of the atmosphere (TOA), tropopause (TRP) and at the surface (SRF). Values are calculated from the difference in the radiative effect of the species in the PD and the PI case. The last row gives the sum of all individual forcings. Comparison with the last row of Table 7 shows that the impact of nonlinearity for the halocarbons is very small.

Species	PI conc. [ppt]	PD conc. [ppt]	TOA [mW m^{-2}]	TRP[mW m^{-2}]	SRF[mW m^{-2}]
Chlorofluorocarbons					
CFC11	0.000	233.080	95.094	82.508	67.669
CFC12	0.000	520.581	256.590	220.217	186.051
CFC113	0.000	72.711	34.564	30.684	24.012
CFC114	0.000	16.307	7.226	6.511	5.240
CFC115	0.000	8.429	2.609	2.250	1.637
Hydrochlorofluorocarbons					
HCFC22	0.000	229.542	73.640	64.262	50.427
HCFC141b	0.000	23.809	5.766	5.157	3.600
HCFC142b	0.000	22.076	6.346	5.421	4.292
Hydrofluorocarbons					
HFC23	0.000	26.890	8.142	6.961	5.229
HFC32	0.000	8.337	1.372	1.226	1.021
HFC125	0.000	15.355	5.628	4.800	3.031
HFC134a	0.000	80.516	21.055	18.166	12.339
HFC143a	0.000	15.253	3.994	3.388	2.091
HFC152a	0.000	7.733	1.451	1.255	0.996
HFC227ea	0.000	1.006	0.411	0.354	0.218
HFC236fa	0.000	0.131	0.049	0.042	0.025
HFC245fa	0.000	2.047	0.770	0.671	0.465
HFC365mfc	0.000	0.765	0.272	0.233	0.153
HFC4310mee	0.000	0.247	0.126	0.110	0.069
Chlorocarbons and Hydrochlorocarbons					
CH3CCl3	0.000	3.680	0.325	0.323	0.176
CCl4	0.025	83.070	20.699	18.461	10.819
CH3Cl	457.000	539.542	0.210	0.293	0.024
CH2Cl2	6.913	36.348	1.879	1.777	0.858
CHCl3	6.000	9.902	0.704	0.632	0.382
Bromocarbons, Hydrobromocarbons and Halons					
CH3Br	5.300	6.686	0.007	0.006	0.004
Halon1211	0.004	3.754	1.787	1.538	1.278
Halon1301	0.000	3.298	1.552	1.334	0.996
Halon2402	0.000	0.431	0.206	0.184	0.132
Fully Fluorinated Species					
NF3	0.000	1.240	0.372	0.322	0.281
SF6	0.000	8.221	6.886	5.877	4.999
SO2F2	0.000	2.039	0.630	0.554	0.402
CF4	34.050	81.092	5.458	4.981	1.041
C2F6	0.000	4.399	1.674	1.444	0.823
C3F8	0.000	0.601	0.208	0.196	0.120
cC4F8	0.000	1.339	0.632	0.540	0.378
C4F10	0.000	0.179	0.095	0.082	0.048
C5F12	0.000	0.126	0.073	0.064	0.036
C6F14	0.000	0.279	0.183	0.159	0.087
C8F18	0.000	0.091	0.069	0.060	0.032
Sum total	—	—	568.755	493.041	391.479

Table 7. Major components of present-day instantaneous clear-sky radiative forcing. Columns 2 and 3 give the pre-industrial (PI) and present-day (PD) concentration, respectively. Remaining columns give the instantaneous clear-sky forcing (difference between PD and PI net fluxes) at the top of the atmosphere (TOA), tropopause (TRP) and at the surface (SRF). Values are calculated from the difference between the present-day references case and an atmosphere where the respective concentration has been replaced by its preindustrial value. Note in particular that for the halocarbons all their concentrations are changed at the same time. Also, total is the effect of changing all species concentrations at once from PD to PI, not the sum of the individual forcings. This table can be compared directly to the middle block of Table 2 in Pincus et al. (2020). For O_3, the concentration depends on location and altitude; the given concentration values are air density-weighted vertical means of the volume mixing ratio, weight-averaged over the 100 atmospheric cases.

Species	PI conc. [ppm]	PD conc. [ppm]	TOA [Wm^{-2}]	TRP [Wm^{-2}]	SRF [Wm^{-2}]
Total	—	—	2.877	4.277	2.023
CO_2	284	397	1.306	2.425	0.913
CH_4	0.808	1.831	0.608	0.663	0.272
N_2O	0.273	0.327	0.203	0.224	0.0850
O_3	1.901	1.813	0.127	0.403	0.316
Halocarbons	—	—	0.573	0.496	0.394

using an earlier halocarbon absorption model based on the convolution method (compare Section 2.2).

It is interesting to look at the level of agreement between our calculation here and the six benchmark model mean in (Pincus et al., 2020). For the present-day instantaneous clear-sky longwave forcing at the TOA, the differences (ARTS minus multi-model mean) are CO_2: -0.2%, CH_4: -0.8%, N_2O: -1.0%, O_3: -1.6%, halocarbons: +7.3%. So, indeed, the only major difference is in the halocarbons, confirming that it was worthwhile to investigate them more closely. A possible interpretation of the approximately 7% difference is that at least some of the other RFMIP models presently underestimate the halocarbon forcing. This may be due to different representations of concentration change (all gases individually versus using equivalent concentrations), or due to some models not having implemented all of the halocarbon species in the case of the explicit treatment.

Overall, halocarbons are responsible for a substantial share of the present-day forcing, $0.573\,Wm^{-2}$ (instantaneous clear-sky at the TOA), corresponding to approximately

20% of the total anthropogenic forcing, or 44% compared to anthropogenic CO_2 forcing alone.

4 Summary and Conclusions

A new and simple model of halocarbon absorption has been developed. It is constructed by applying second order polynomial fits in pressure and temperature to HITRAN absorption cross-section data. The model reduces to the case without pressure and/or temperature dependence for gas species where data coverage is inadequate to do a fit.

The model was implemented and tested in the Atmospheric Radiative Transfer Simulator (ARTS), but was intentionally constructed so that it is very easy to use stand-alone or in other radiative transfer models: Polynomial coefficients are stored in data files, and the formula to apply them is given in this article, in the ARTS source code, and in stand-alone Python code (see Section 5).

Currently, the model is implemented for 37 of the 40 halocarbon species requested by RFMIP/CMIP (we model CH_3Cl and CH_3Br explicitly from spectral line data and completely omit C_7F_{16}, for which HITRAN has no data). It could easily be extended to other gases, to the extent that cross-section data are available.

The model improves on previously available options for using spectral cross-sections, which were to use the cross-section data for particular pressure / temperature conditions directly (ignoring the dependencies), as in Hod20, to do an explicit (temperature) interpolation of the cross-section data inside the RT code, as in MODTRAN (Berk et al., 2005), to use an algorithmic model with looser connection to the cross-section data, as in LBLRTM (Clough et al., 2005), or to use a pseudo-line list available only for selected species, as in SFIT (Hase et al., 2004). In particular, in our approach it is completely transparent how the model is constructed from the data, all species are treated consistently, and the available data are fully exploited.

Such a model has many applications, for example in remote sensing, in generating k-distributions for circulation model radiation schemes, and in calculating radiative energy fluxes. In the last of these areas we presented an application in this article, namely the estimation of radiative efficiency and present-day radiative forcing of the different halocarbon species. Results for radiative efficiency are broadly consistent with the re-

cent assessment by Hod20, within approximately 10%. A larger discrepancy for one species (57% for CH_3Br) that we have modeled from explicit spectroscopic line parameters, not the new absorption model, was found to be due to incomplete HITRAN line data.

For the other gas species, part of the differences can be explained by the lacking treatment of temperature dependence in Hod20. Slightly different values of the integrated absorption band strength S due to inconsistencies of HITRAN data at different temperature also play a role for a few species. Remaining differences unexplained by these two factors likely are due to the crude cloud correction that we have done for the sake of comparison to the Hod20 all-sky values, and due to the different assumed atmospheric states (100 RFMIP atmospheres versus 2 Hod20 atmospheres).

An added value of our new analysis is that we quantify the impact of the temperature dependence for all gas species where the laboratory data allow it. We find the difference in radiative efficiency to be significant — in some cases, up to approximately 8%. The impact could be even stronger for some of the species where data coverage is too poor to do the temperature fit, the best example being Halon1301. This stresses the need for more laboratory measurements at low temperatures. Data at different temperatures are not informative if the temperature range is narrow relative to the range of temperatures in the atmosphere: Data down to 280 K, as for Halon1301 are not enough, they should reach down to below 200 K, as for CFC11.

Our direct simulations with the new halocarbon absorption model confirm the substantial present-day radiative forcing by halocarbons that was already reported by earlier assessments. Although the effect is spread over many different compounds, and the contribution of each individual compound is relatively small, three compounds stick out: The largest individual contributions are by CFC12 (257 $\mathrm{mW\,m^{-2}}$ instantaneous clear-sky forcing at the top of the atmosphere), CFC11 (95 $\mathrm{mW\,m^{-2}}$) and HCFC22 (74 $\mathrm{mW\,m^{-2}}$). Together, these three compounds are responsible for almost 75% of the sum-total of the haloncarbon forcings. In this context it is worrying that observations indicate that atmospheric CFC11 concentrations are not decreasing as fast as expected based on the Montreal Protocol (see Chen et al., 2020, and references therein).

5 Code and Data Availability

The absorption model coefficients are published in NetCDF format on Zenodo (`https://zenodo.org/record/6542793`). These coefficients are generated with the ARTS-crossfit software package which is available on Github (`https://github.com/atmtools/arts-crossfit/releases/tag/v1.0.0`). For reproducibility, the version of ARTS that was used for the calculations in this article can be retrieved from Github (`https://github.com/atmtools/arts/tree/c0cc180d`). For other calculations, the use of version 2.5.4 or later (`https://github.com/atmtools/arts/releases`) is recommended since the ARTS model is continuously developed and improved.

6 Acknowledgements

An earlier version of the new absorption model was evaluated and compared against LBLRTM by Hanna Dunke in the context of her bachelor's thesis. We thank Eli Mlawer for providing the LBLRTM results for that exercise. Furthermore, we would like to acknowledge the general support from the ARTS developer and user community. This work contributes to the Cluster of Excellence Climate, Climatic Change, and Society (CLICCS) and to the Center for Earth System Research and Sustainability (CEN) of Universität Hamburg. This work was partly supported by the US National Oceanic and Atmospheric Administration under award NA2OAR4310375.

References

Bak, J., Liu, X., Birk, M., Wagner, G., Gordon, I. E., & Chance, K. (2020). Impact of using a new ultraviolet ozone absorption cross-section dataset on OMI ozone profile retrievals. *Atmos. Meas. Tech.*, *13*(11), 5845–5854. Retrieved from `https://amt.copernicus.org/articles/13/5845/2020/` doi: 10.5194/amt-13-5845-2020

Berk, A., Anderson, G. P., Acharya, P. K., Bernstein, L. S., Muratov, L., Lee, J., ... Gardner, J. A. (2005). MODTRAN5: a reformulated atmospheric band model with auxiliary species and practical multiple scattering options. In A. M. Larar, M. Suzuki, & Q. Tong (Eds.), *Multispectral and hyperspectral remote sensing instruments and applications ii* (Vol. 5655, pp. 88–95). SPIE. Retrieved from `https://doi.org/10.1117/12.578758` doi: 10.1117/12.578758

Buehler, S. A., Eriksson, P., Kuhn, T., von Engeln, A., & Verdes, C. (2005, Febru-

ary). ARTS, the atmospheric radiative transfer simulator. *J. Quant. Spectrosc. Radiat. Transfer*, *91*(1), 65–93. doi: 10.1016/j.jqsrt.2004.05.051

Buehler, S. A., Mendrok, J., Eriksson, P., Perrin, A., Larsson, R., & Lemke, O. (2018). ARTS, the atmospheric radiative transfer simulator — version 2.2, the planetary toolbox edition. *Geosci. Model Dev.*, *11*(4), 1537–1556. doi: 10.5194/gmd-11-1537-2018

Chen, X., Huang, X., & Strow, L. L. (2020). Near-global CFC-11 trends as observed by atmospheric infrared sounder from 2003 to 2018. *J. Geophys. Res.: Atm.*, *125*(22), 1–14. doi: 10.1029/2020JD033051

Clough, S. A., Shephard, M. W., Mlawer, E. J., Delamere, J. S., Iacono, M., Cady-Pereira, K., ... Brown, P. D. (2005). Atmospheric radiative transfer modeling: a summary of the AER codes. *J. Quant. Spectrosc. Radiat. Transfer*, *91*(2), 233–244. doi: 10.1016/j.jqsrt.2004.05.058

Eriksson, P., Buehler, S. A., Davis, C. P., Emde, C., & Lemke, O. (2011). ARTS, the atmospheric radiative transfer simulator, version 2. *J. Quant. Spectrosc. Radiat. Transfer*, *112*(10), 1551–1558. doi: 10.1016/j.jqsrt.2011.03.001

Eyring, V., Bony, S., Meehl, G. A., Senior, C. A., Stevens, B., Stouffer, R. J., & Taylor, K. E. (2016). Overview of the Coupled Model Intercomparison Project Phase 6 (CMIP6) experimental design and organization. *Geosci. Model Dev.*, *9*(5), 1937–1958. doi: 10.5194/gmd-9-1937-2016

Gordon, I. E., Rothman, L. S., Hargreaves, R. J., Hashemi, R., Karlovets, E. V., Skinner, F. M., ... Yurchenko, S. (2022, January). The HITRAN2020 molecular spectroscopic database. *J. Quant. Spectrosc. Radiat. Transfer*, *277*, 107949. Retrieved from `https://linkinghub.elsevier.com/retrieve/pii/S0022407321004416` doi: 10.1016/j.jqsrt.2021.107949

Gordon, I. E., Rothman, L. S., Hill, C., Kochanov, R. V., Tan, Y., Bernath, P. F., ... Zak, E. J. (2017, September). The HITRAN2016 molecular spectroscopic database. *J. Quant. Spectrosc. Radiat. Transfer*, 1–66. doi: 10.1016/j.jqsrt.2017.06.038

Harrison, J. J. (2018, October). New and improved infrared absorption cross sections for trichlorofluoromethane (CFC-11). *Atmos. Meas. Tech.*, *11*(10), 5827–5836. doi: 10.5194/amt-11-5827-2018

Hase, F., Hannigan, J. W., Coffey, M. T., Goldman, A., Höpfner, M., Jones, N. B.,

... Wood, S. W. (2004). Intercomparison of retrieval codes used for the analysis of high-resolution, ground-based FTIR measurements. *J. Quant. Spectrosc. Radiat. Transfer*, *87*(1), 25–52. doi: 10.1016/j.jqsrt.2003.12.008

Hodnebrog, Ø., Aamaas, B., Fuglestvedt, J. S., Marston, G., Myhre, G., Nielsen, C. J., ... Wallington, T. J. (2020). Updated global warming potentials and radiative efficiencies of halocarbons and other weak atmospheric absorbers. *Rev. Geophys.*, *58*(3), 1–30. doi: 10.1029/2019RG000691

Hodnebrog, Ø., Etminan, M., Fuglestvedt, J. S., Marston, G., Myhre, G., Nielsen, C. J., ... Wallington, T. J. (2013). Global warming potentials and radiative efficiencies of halocarbons and related compounds: A comprehensive review. *Rev. Geophys.*, *51*(2), 300–378. doi: 10.1002/rog.20013

Hodnebrog, Ø., Myhre, G., Kramer, R. J., Shine, K. P., Andrews, T., Faluvegi, G., ... Voulgarakis, A. (2020). The effect of rapid adjustments to halocarbons and N_2O on radiative forcing. *npj Clim. Atm. Sci.*, *3*(43). doi: 10.1038/s41612-020-00150-x

Huang, Y., Tan, X., & Xia, Y. (2016). Inhomogeneous radiative forcing of homogeneous greenhouse gases. *J. Geophys. Res.: Atm.*, *121*(6), 2780–2789. doi: 10.1002/2015JD024569

Jacquinet-Husson, N., Armante, R., Scott, N., Chédin, A., Crépeau, L., Boutammine, C., ... Makie, A. (2016). The 2015 edition of the geisa spectroscopic database. *J. Molec. Struct.*, *327*, 31–72. Retrieved from `https://www.sciencedirect.com/science/article/pii/S0022285216301011` (New Visions of Spectroscopic Databases, Volume II) doi: https://doi.org/10.1016/j.jms.2016.06.007

Johnson, T. J., Profeta, L. T. M., Sams, R. L., Griffith, D. W. T., & Yokelson, R. L. (2010, May). An infrared spectral database for detection of gases emitted by biomass burning. *Vib. Spectrosc.*, *53*(1), 97–102. doi: 10.1016/j.vibspec.2010.02.010

Kochanov, R. V., Gordon, I. E., Rothman, L. S., Sharpe, S. W., Johnson, T. J., & Sams, R. L. (2015). Comment on "Radiative forcings for 28 potential Archean greenhouse gases" by Byrne and Goldblatt (2014). *Clim. Past*, *11*(8), 1097–1105. Retrieved from `https://cp.copernicus.org/articles/11/1097/2015/` doi: 10.5194/cp-11-1097-2015

Kochanov, R. V., Gordon, I. E., Rothman, L. S., Shine, K. P., Sharpe, S. W., Johnson, T. J., ... Hill, C. (2019). Infrared absorption cross-sections in hitran2016 and beyond: Expansion for climate, environment, and atmospheric applications. *J. Quant. Spectrosc. Radiat. Transfer*, *230*, 172–221. doi: 10.1016/j.jqsrt.2019.04.001

Meinshausen, M., Vogel, E., Nauels, A., Lorbacher, K., Meinshausen, N., Etheridge, D. M., ... Weiss, R. (2017). Historical greenhouse gas concentrations for climate modelling (CMIP6). *Geosci. Model Dev.*, *10*(5), 2057–2116. Retrieved from `https://gmd.copernicus.org/articles/10/2057/2017/` doi: 10.5194/gmd-10-2057-2017

Mlawer, E. J., Payne, V. H., Moncet, J.-L., Delamere, J. S., Alvarado, M. J., & Tobin, D. C. (2012). Development and recent evaluation of the MT_CKD model of continuum absorption. *Phil. Trans. R. Soc. A*, *370*(1968), 2520–2556.

Myhre, G., Stordal, F., Gausemel, I., Nielsen, C. J., & Mahieu, E. (2006). Line-by-line calculations of thermal infrared radiation representative for global condition: CFC-12 as an example. *J. Quant. Spectrosc. Radiat. Transfer*, *97*(3), 317–331. doi: 10.1016/j.jqsrt.2005.04.015

Pincus, R., Buehler, S. A., Brath, M., Crevoisier, C., Jamil, O., Evans, K. F., ... Tellier, Y. (2020). Benchmark calculations of radiative forcing by greenhouse gases. *J. Geophys. Res.: Atm.*, *123*(23), e2020JD033483. doi: 10.1029/2020JD033483

Pincus, R., Forster, P. M., & Stevens, B. (2016). The radiative forcing model intercomparison project (RFMIP): experimental protocol for CMIP6. *Geosci. Model Dev.*, *9*(9), 3447–3460. Retrieved from `https://www.geosci-model-dev.net/9/3447/2016/` doi: 10.5194/gmd-9-3447-2016

Pinnock, S., Hurley, M. D., Shine, K. P., Wallington, T. J., & Smyth, T. J. (1995). Radiative forcing of climate by hydrochlorofluorocarbons and hydrofluorocarbons. *J. Geophys. Res.: Atm.*, *100*(D11), 23227–23238. doi: 10.1029/95JD02323

Rinsland, C. P., Goldman, A., Murcray, D. G., Murcray, F. J., Bonomo, F. S., Blatherwick, R. D., ... Rinsland, P. L. (1985). Tentative identification of the 780-cm^{-1} ν_4 band q branch of chlorine nitrate in high-resolution solar absorption spectra of the stratosphere. *J. Geophys. Res.*, *90*(D5), 7931–7943.

Retrieved from https://agupubs.onlinelibrary.wiley.com/doi/abs/10.1029/JD090iD05p07931 doi: https://doi.org/10.1029/JD090iD05p07931

Sharpe, S. W., Johnson, T. J., Sams, R. L., Chu, P. M., Rhoderick, G. C., & Johnson, P. A. (2004). Gas-phase databases for quantitative infrared spectroscopy. *Appl. Spectrosc.*, *58*(12), 1452-1461. doi: 10.1366/0003702042641281

Shine, K., & Myhre, G. (2020). The spectral nature of stratospheric temperature adjustment and its application to halocarbon radiative forcing. *J. Adv. Model. Earth Syst.*, *12*(3), e2019MS001951. Retrieved from https://agupubs.onlinelibrary.wiley.com/doi/abs/10.1029/2019MS001951 (e2019MS001951 2019MS001951) doi: https://doi.org/10.1029/2019MS001951

Soden, B. J., & Held, I. M. (2006). An assessment of climate feedbacks in coupled ocean-atmosphere models. *J. Climate*, *19*(14), 3354–3360. doi: 10.1175/JCLI3799.1